Supplementary Information for

Coexistence of chiral phonons and antiferroelectricity in breathing kagome semiconductor Nb_3I_8 at room-temperature

Jin Hong[1,#], Fengrui Sui[1,#], Kaiqi Wang[1,#], Xin Han[2,#], Yufan Zheng[1], Wen-yi Tong[1], Xing Deng[1], Zhao, Guan[1], Bobo Tian[1], Ruijuan Qi[1*], Rong Huang[1], Ni Zhong[1], Hui Peng[1], Fangyu Yue[1,3*], Junhao Chu[1,4], Youguo Shi[2*] & Chungang Duan[1,3*]

[1]Key Laboratory of Polar Materials and Devices (MOE), Shanghai Center of Brain-inspired Intelligent Materials and Devices, Department of Electronics, East China Normal University, Shanghai 200241, China.

[2]Beijing National Laboratory for Condensed Matter Physics and Institute of Physics, Chinese Academy of Sciences, Beijing 100190, China.

[3]Collaborative Innovation Center of Extreme Optics, Shanxi University, Taiyuan, Shanxi 030006, China.

[4]National Laboratory of Infrared Physics, Shanghai Institute of Technical Physics, Shanghai 200083, China.

[#]They equally contribute to this work.

* Email: rjqi@ee.ecnu.edu.cn; fyyue@ee.ecnu.edu.cn; ygshi@iphy.ac.cn; cgduan@clpm.ecnu.edu.cn

This supplementary information consists of 4 sections in support of the main text. The contents of the sections are listed below:

1. **Additional information about the microstructure of Nb_3I_8 crystal**
2. **Band structures and polarized Raman spectra of Nb_3I_8**
3. **Verifying the ferroelectricity in Nb_3I_8**
4. **Polarization switching in monolayer and bilayer Nb_3I_8**

Section 1. Additional information about the microstructure of Nb_3I_8 crystal

2D Nb_3I_8 crystal stabilizes as layered structure at room temperature (Fig. S1a) with the chemical composition of Nb:I≈3:8 (Fig. S1b). However, it is extremely ambient-sensitive when being thinned down or prepared to be TEM lamellae. We adopt effective approaches to obtain HAAD-STEM images of Nb_3I_8, such as short exposure time to air and low probe voltage during image acquiring. In addition, to verify the atomic configurations of Nb_3I_8, we perform detailed simulations on HAADF-STEM images for different thick Nb_3I_8 along both [100] and [001] zone axes (Fig. S2). Simulated results are well consistent with our experiments. Also, the alternating vdWs gaps at atomic-scale in Nb_3I_8 are simulated along [100] and [120] zone axes, respectively (Fig. S3).

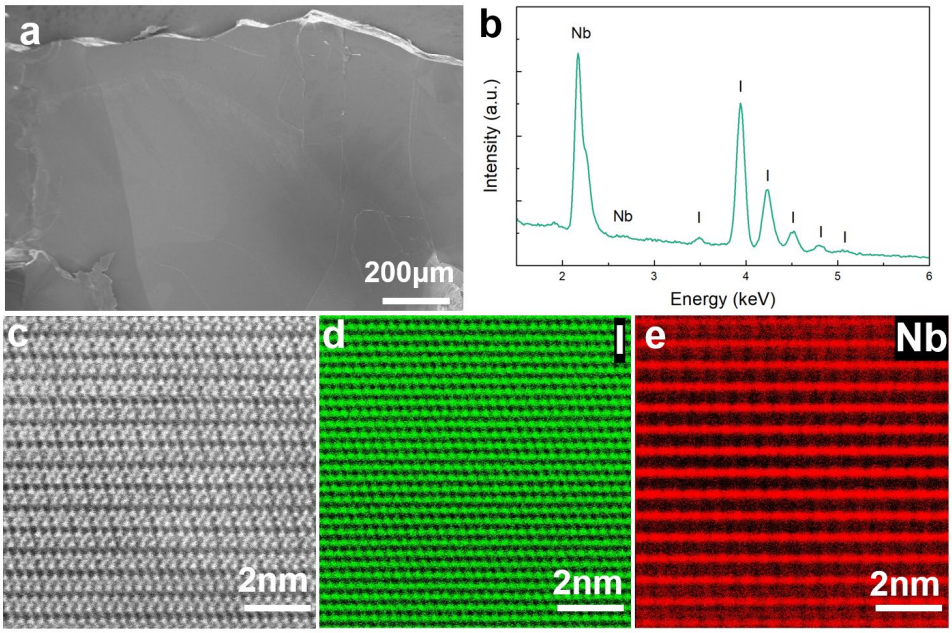

Supplementary Fig. 1 | SEM image and chemical composition of Nb_3I_8. a, SEM image. **b**, SEM-EDS spectrum. **c-e**, HAADF-STEM image and corresponding EDS maps of Nd and iodine atoms.

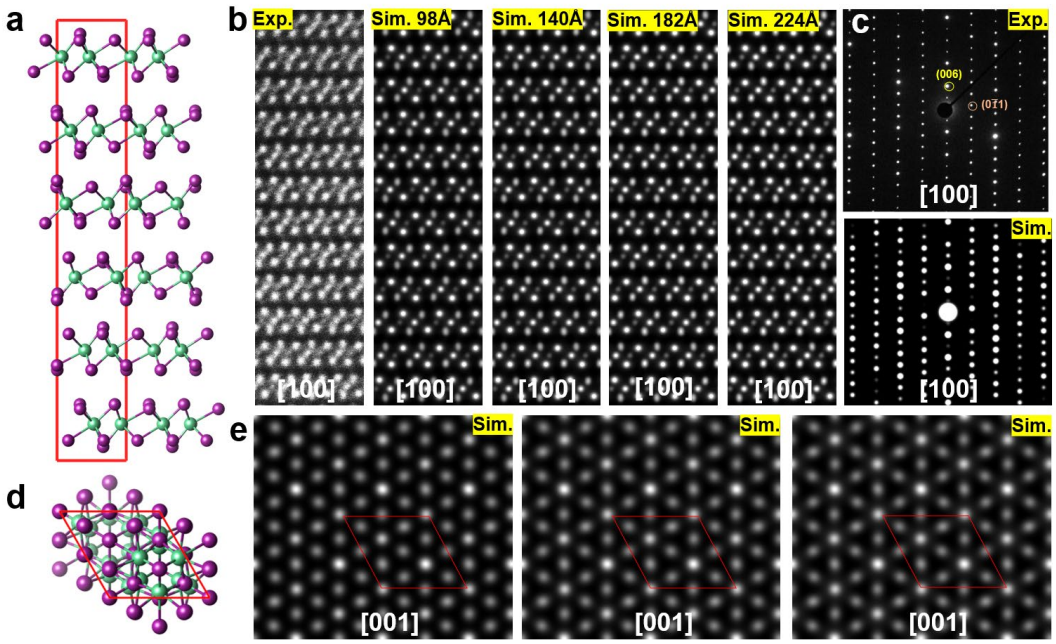

Supplementary Fig. 2 | Crystal structure schematics of Nb_3I_8. a, Side view of Nb_3I_8 unit cell. **b**, Simulated HAADF-STEM images along [100] zone axis. **c**, SAED patterns of Nb_3I_8 along [100] zone axis. **d**, Top view of Nb_3I_8 unit cell. **e**, Simulated HAADF-STEM images along [001] zone axis.

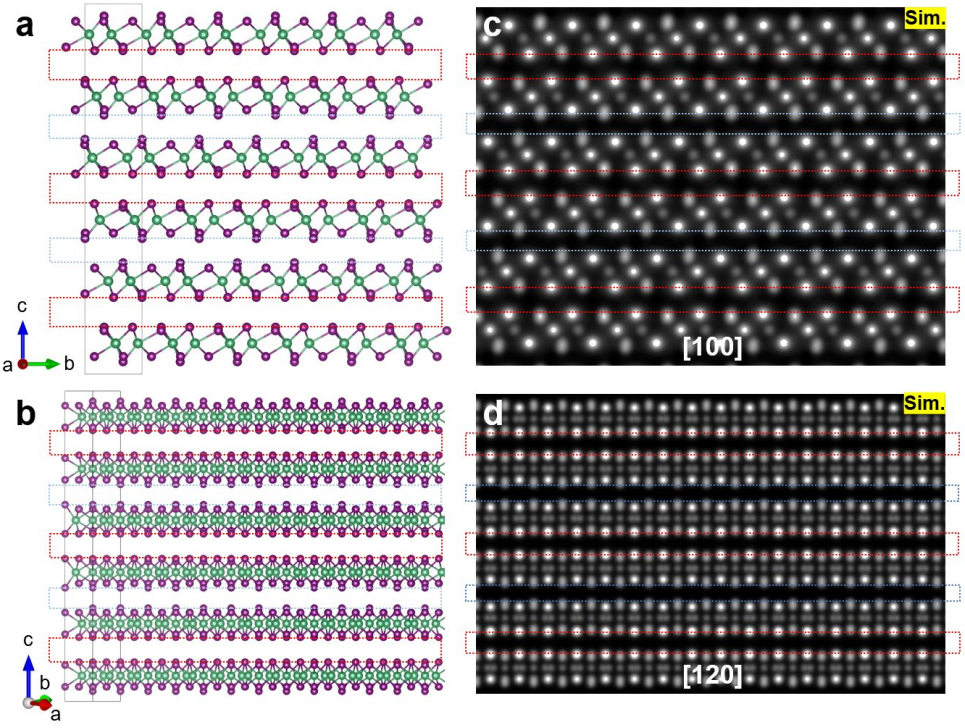

Supplementary Fig. 3 | VdWs gaps arrangements with alternating distances at atomic-scale in Nb_3I_8. a and **b**, Side-views of the crystal structure along [100] and [120] zone axes. **c** and **d**,

Corresponding simulated HAADF-STEM images along [100] and [120] zone axes.

Section 2. Band structures and polarized Raman spectra of Nb_3I_8

Tunable optical bandgap of Nb_3I_8 in infrared waveband

As mentioned in the main text, bulk Nb_3I_8 is indirect with an optical bandgap of ~0.22 eV. Here, considering the interlayer antiferromagnetic configuration of bulk phase, we calculate the spin-resolved band structure of bulk Nb_3I_8, as shown in Fig. 4a. The band dispersion of bulk phase of spin up and spin down are almost coincident, giving an indirect bandgap of ~0.38 eV. When the flake is thinned down to monolayer, the ferrovalley feature would appear, as shown in Fig. S4b, c for the calculated results. Considering the ferromagnetic configuration of monolayer Nb_3I_8, first-principles calculations show spin-resolved band structures with two direct optical transitions around 1.0 eV in K+ and K- valleys, consistent with the report[1]. Notice that our thinned nanoflakes give an optical bandgap of ~0.68 eV by optical transmission spectroscopy. Thus, the tunable optical bandgap of Nb_3I_8 in infrared waveband is revealed by our experimental and calculated results.

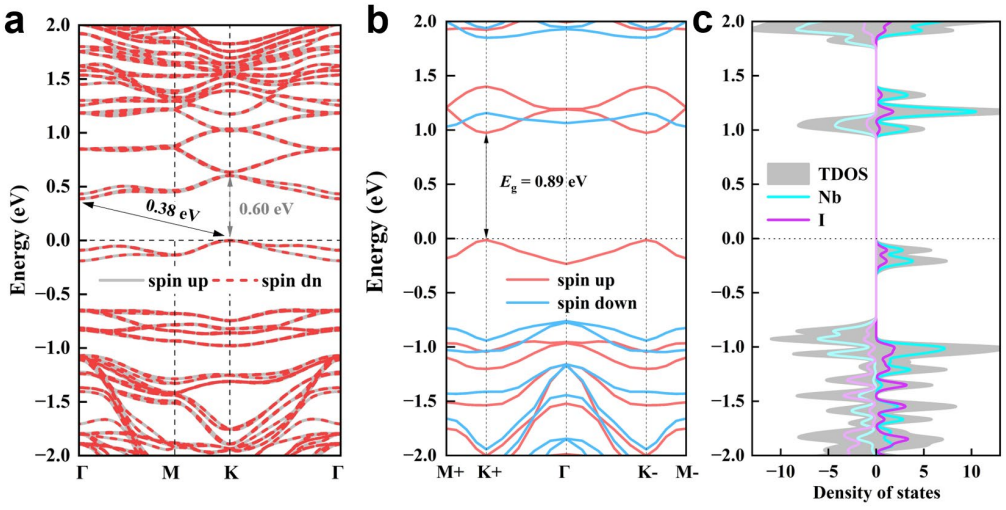

Supplementary Fig. 4 | Band structure of Nb_3I_8. a and **b**, Spin-polarized band structures of bulk (a) and monolayer (b). **c**, Corresponding density of states of monolayer Nb_3I_8.

Linearly and circularly polarized Raman: Optical setup and results

The schematic of optical setup for linearly polarized Raman (LPR) is displayed in Fig. S5a, while that for circularly polarized Raman (CPR) is shown in Fig. S5b. For the LPR measurements, a linear polarizer (LP_1) is placed in the incident path to achieve x direction polarization, while another broadband linear polarizer (LP_2) is in front of detector for backscattered Raman signal analysis. The LP_2 can be rotated at different angles to obtain the 360° angle-dependent LPR spectra. For the CPR measurements, a quarter-wave plate is placed behind LP_1 in the incident path to achieve the right (σ+) or left (σ-) circular polarization, while another quarter-wave plate is placed in front of LP_2 for the helicity of backscattered Raman signal analysis. The σ+ (or σ-) incident light is confirmed at the sample position. The σ- or σ+ polarizations in front of detector are employed to check the helicity of the scattered photons. We rotate the quarter-wave plate in front of LP_2 to complete the angle-dependent CPR measurements. We verify the effectivity of our optical setup by referring to the CPR spectra of a MoS_2 flake with a thickness of ~15 nm (Fig. S5c). Fig. S5d shows the room-temperature CPR spectrum of a MoS_2 flake in $z(\sigma+,\sigma+)\bar{z}$ and $z(\sigma+,\sigma-)\bar{z}$ geometric configurations. It is clear that the OC phonon scattered photons have the same σ+ helicity as the incident photons (bule curve), while the IMC phonon peak is obviously enhanced under the opposite (σ-) polarization (red curve), totally consistent with the previous report[2], proving the reliability of the optical setup. Subsequently, we perform the angle-dependent LPR and CPR measurements on bulk Nb_3I_8. As presented in Fig. S6a, the Raman peaks of A_{1g} modes are continuously weakened till to disappear when the LP_2 is rotated from 0° to 90°. For the angle-dependent CPR results (Fig. S6b), the Raman signals of E_g modes gradually increase to maximum when the geometries are switched from $z(\sigma+,\sigma+)\bar{z}$ (0°) to $z(\sigma+,\sigma-)\bar{z}$ (90°). The peak positions of A_{1g} and E_g modes are consistent with our first-principles calculations (Fig. S6c).

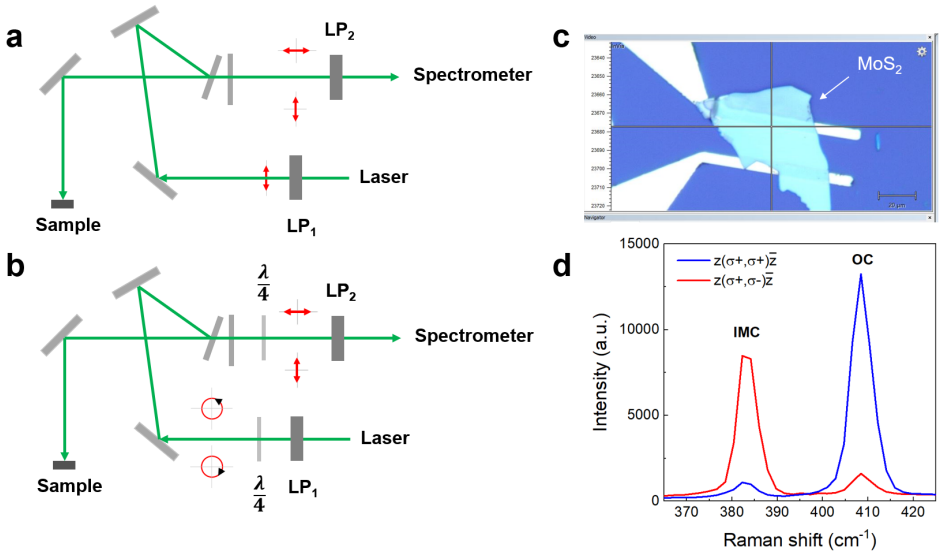

Supplementary Fig. 5 | Schematic of optical setup for polarized Raman measurements. a and **b**, Optical setup for LPR (a) and CPR (b) spectroscopy. **c**, Morphology of the MoS_2 flake with a thickness of ~15 nm. **d**, Room-temperature CPR spectrum of the MoS_2 flake in (c) in $z(\sigma+,\sigma+)\bar{z}$ and $z(\sigma+,\sigma-)\bar{z}$ geometric configurations.

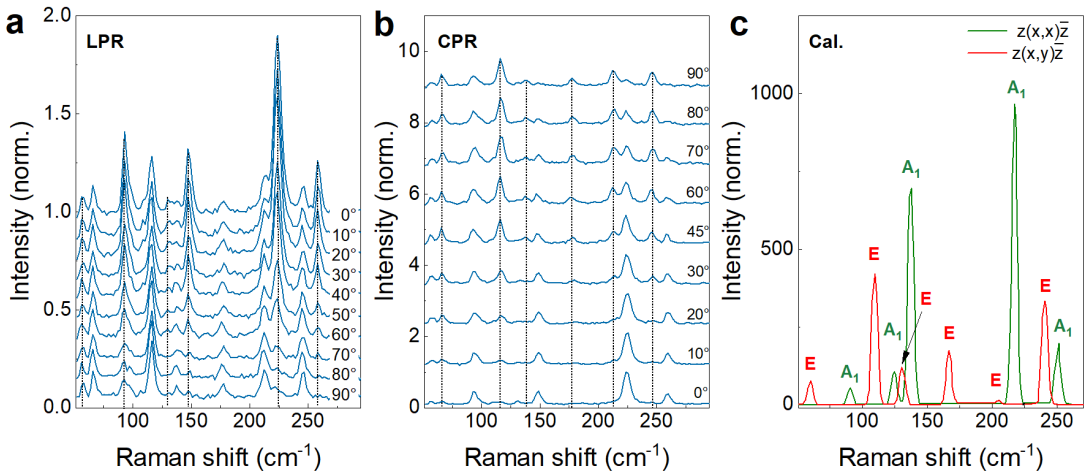

Supplementary Fig. 6 | Experimental and calculated Raman spectra of Nb_3I_8. a and **b**, Angle-dependent LPR (a) and CPR (b) spectra. The initial 0° in angle-dependent LPR and CPR measurements, respectively, represent the $z(x,x)\bar{z}$ and $z(\sigma+,\sigma-)\bar{z}$ configurations. The dashed lines in **a** and **b** identify the achiral and chiral modes, respectively. **c**, Calculated Raman spectra of monolayer Nb_3I_8 in $z(x,x)\bar{z}$ and $z(x,y)\bar{z}$ configurations.

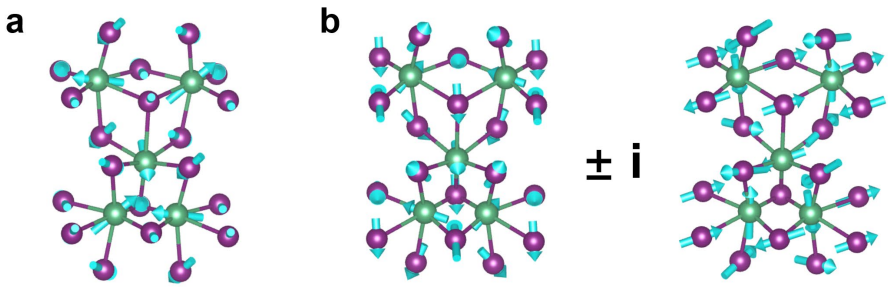

Supplementary Fig. 7 | Phonon eigenvectors with calculated frequencies of achiral and chiral modes at the Brillouin zone center in Nb_3I_8. a and **b**, The Nb and I atomic vibrations of A_{1g}^4 (a) and E_g^3 (b) modes. Note that superposition of two orthogonal linear vibrations of E_g^3 results in right-handed or left-handed circular motions at the Γ-point.

Section3. Verifying the ferroelectricity in Nb_3I_8

Hysteresis loop measurements by piezoresponse force microscopy (PFM) have regarded as a powerful technique for probing polarization switching in nanoscale[3-5]. As known, a ferroelectric material possessing spontaneous polarization that can be reversed by the external electric field, which will show switchable local PFM amplitude and 180° phase loops. Here, the electric-field induced ferroelectricity in Nb_3I_8 has been verified on different thick flakes (Fig. S8a-c and Fig. S9). The out-of-plane effective piezoelectric constant (d_{33}^{eff}) for different thicknesses in the as-prepared Nb_3I_8 nanoflakes are calculated (Fig. S8d).

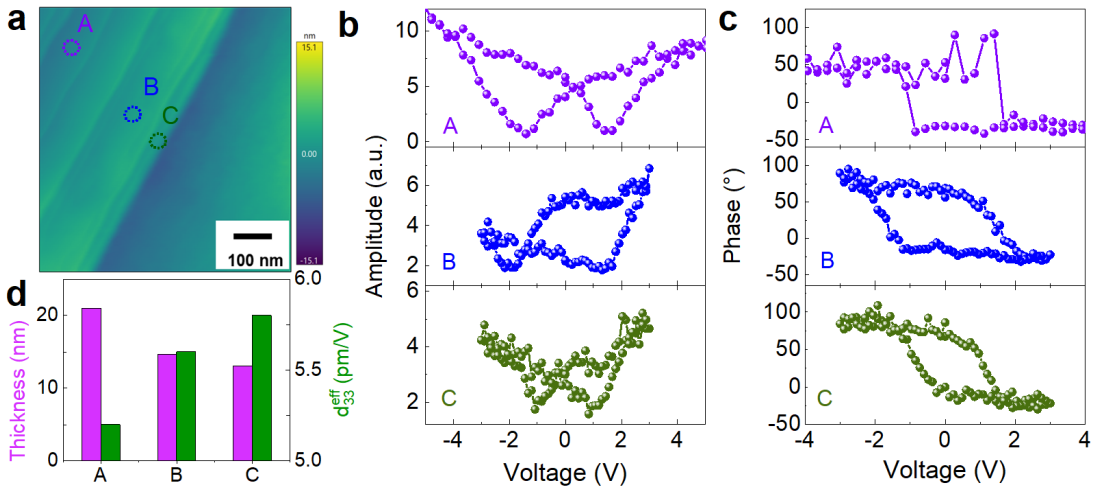

Supplementary Fig. 8 | Additional PFM results of Nb_3I_8 flakes with different thicknesses. a, Morphology of the exfoliated Nb_3I_8 flake with stepped shape, where the regions marked by A, B, and C represent different thicknesses. **b** and **c**, Local PFM amplitude (b) and PFM phase (c) hysteresis loops from the A, B, and C regions. **d**, The determined thicknesses (purple) and calculated d_{33}^{eff}-values (green) for A, B, and C regions.

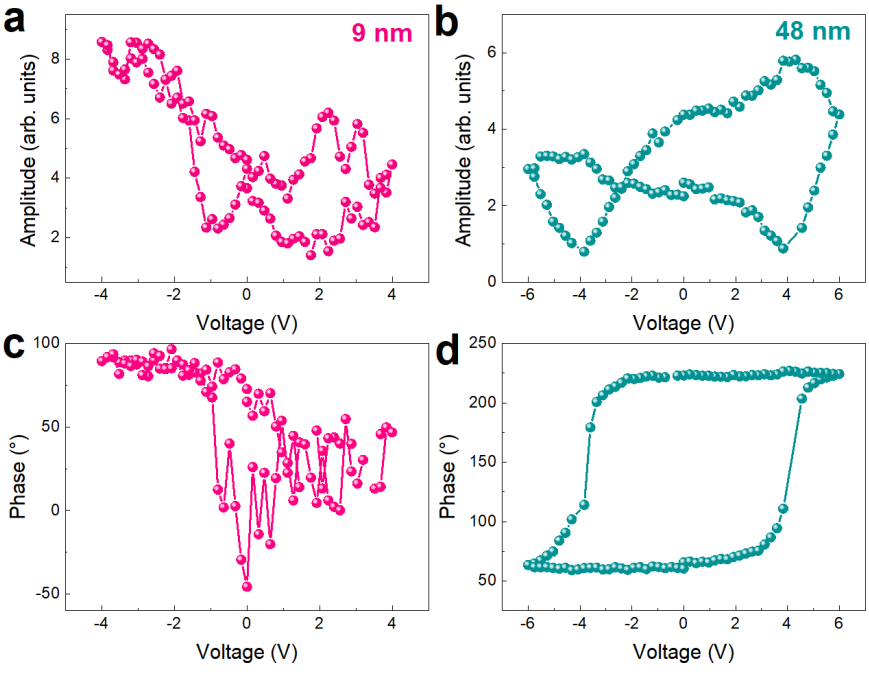

Supplementary Fig. 9 | Additional PFM results of Nb_3I_8 flakes with different thicknesses. a-d, Local PFM amplitude (a, b) and phase (c, d) hysteresis loops of Nb_3I_8 flakes with thickness of ~9 nm and 48 nm, respectively.

Section4. Polarization switching in monolayer and bilayer Nb_3I_8

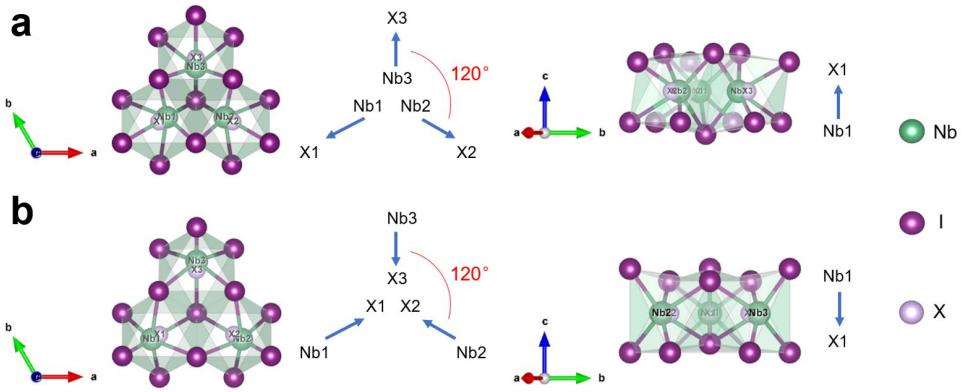

Supplementary Fig. 10 | Electric polarization states of the small and big triangles of Nb_3I_{13} architechtures. a and **b**, Atomic configuration of Nb_3I_{13}, where the X atom represents the center site of the iodine atom in each octahedron. As the angle between any two electric dipole moments is 120 degrees, the net electric dipole moment in a-b plane is zero. However, in the a-c plane, the three octahedra provide an upward dipole moment, which leads to an upward polarization in the Nb_3I_{13} architecture (a) and thus leads to a downward dipole moment in (b). It should be noted that the magnitude of the electric dipole moment in (b) is slightly smaller than that in (a) along c direction.

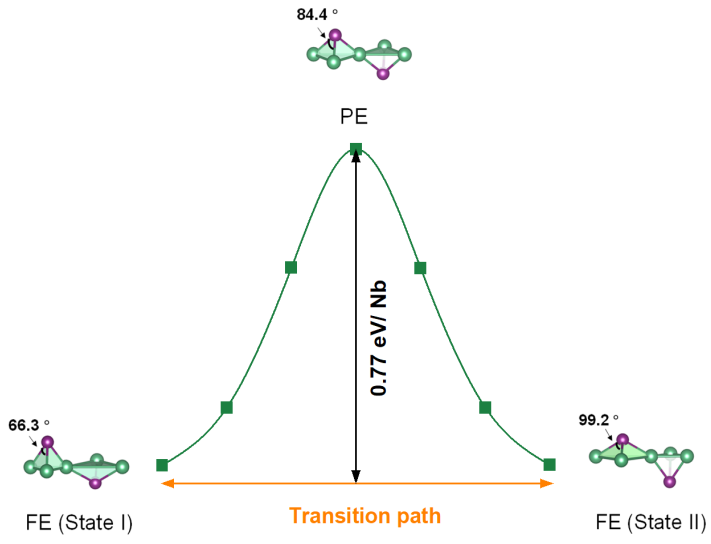

Supplementary Fig. 11 | Kinetic pathway of polarization switching in monolayer Nb_3I_8. The climbing image nudged elastic band (NEB) results of the Nb_3I_8 monolayers for ferroelectric switching path from State I to State II. Two ferroelectric (FE) states and the unstable paraelectric

(PE) state are illustrated by the side views of the tetrahedron structures formed by iodine atoms at the top/bottom apex sites and Nb atoms as triangular bases. The energy barrier is calculated to be ~0.77 eV per Nb atom, consistent with the report[6].

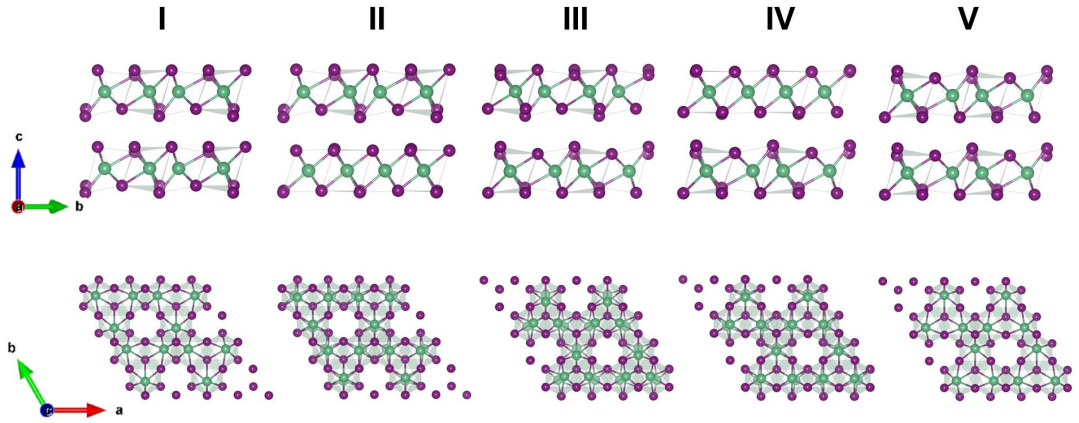

Supplementary Fig. 12 | Structures of five specified states in bilayer Nb_3I_8. Side-views (upper) and top-views (lower) of five states in bilayer Nb_3I_8.

References

1. Peng, R. et al. Intrinsic anomalous valley Hall effect in single-layer Nb_3I_8. *Phys. Rev. B* **102**, 035412 (2020).
2. Chen, S. et al. Helicity-resolved Raman scattering of MoS_2, $MoSe_2$, WS_2, and WSe_2 atomic layers. *Nano Lett*. **15**, 2526-2532 (2015).
3. Strelcov, E. et al. Role of measurement voltage on hysteresis loop shape in piezoresponse force microscopy. *Appl. Phys. Lett.* **101**, 192902 (2012).
4. Vasudevan, R. K. et al. Ferroelectric or non-ferroelectric: Why so many materials exhibit "ferroelectricity" on the nanoscale. *Appl. Phys. Lett.* **4**, 021302 (2017).
5. Guan, Z. et al. Identifying intrinsic ferroelectricity of thin film with piezoresponse force microscopy. *AIP Adv.* **7**, 095116 (2017).
6. Feng, Y. & Yang Q. Enabling triferroics coupling in breathing kagome lattice Nb_3X_8 (X = Cl, Br, I) monolayers. *J. Mater. Chem. C* **11**, 5762-5769 (2023).